PAPER • OPEN ACCESS

Stability of floating objects at a two-fluid interface

View the article online for updates and enhancements.

Stability of floating objects at a two-fluid interface

Daniel M Anderson⬤**, Patrick R Bishop, Mark Brant, Gabriela Castaneda Guzman, Evelyn Sander**⬤ **and Gina Thomas**

Department of Mathematical Sciences, George Mason University, Fairfax, VA 22030, United States of America

E-mail: danders1@gmu.edu

CrossMark

Abstract

We explore the stability of floating objects at a two-fluid interface through mathematical modeling and experimentation. Our models are based on standard ideas of center of gravity, center of buoyancy, and Archimedes' Principle extended to the two-fluid scenario. We investigate floating shapes with uniform, two-dimensional cross sections and identify analytically and/or computationally a potential energy landscape that helps identify stable and unstable floating orientations. We compare our analyses and computations to experiments on floating objects designed and created through 3D printing. Additionally, the paper includes open problems for further study.

Keywords: stability, floating, archimedes' principle, two-fluid interface

1. Introduction

Most students who take a course in Physics encounter Archimedes' Principle. As typically presented, Archimedes' Principle states that *the upward buoyant force on an object fully or partially submerged in a fluid is equal to the weight of the displaced fluid.* Known for more than two millenia, the concept is as essential to historical discussions of fluid physics as it is fundamental to modern marine vessel architecture. It is ubiquitous in everyday life in the kitchen, at the beach, and in most places where solid objects encounter a body of water, large

or small. Archimedes' Principle is the fundamental principle behind standard techniques used in fluid and solid density metrology [1]. For example, in the food science industry, the density of liquids such as milk or alcohol are determined by measuring the volume displaced by a carefully-calibrated hydrometer floating in the liquid. To measure the density of broken glass from a crime scene using the 'sink/float method', forensic scientists submerge glass shards in a fluid of known density and then mix in a more dense fluid drop by drop until the shards become neutrally-buoyant and reveal their precise density [2, 3]. This forensics application is a chemical analog of Galileo's Thermometer, in which thermally-driven density changes exploit Archimedes' Principle to predict temperature.[1] Of course, Archimedes' earliest investigative application determined the volume and then density of a complex shape (i.e. a gold crown).

For freely floating objects, the question of their stability is a fascinating and very rich area for which even relatively simple shapes give rise to surprising complexity. Again the story starts with Archimedes. A modern interpretation of Archimedes' original results on the stability of a floating right paraboloid is beautifully summarized by Rorres [5]. In particular, Rorres presents visualizations of the equilibrium surfaces in a three-dimensional space defined by the relative density of the right paraboloid, its base angle, and its tilt angle (see figures 4 and 5 in that work). These give a modern-day visualization of the stable floating solutions identified by Archimedes as well as Rorres' completion addressing additional cases in which the waterline intersects the base of the paraboloid. Rorres highlights features in these diagrams referred to as 'fold catastrophes' that correspond to events mimicking shape-change (e.g. melting) induced iceberg tumbling as well as soil liquifaction-induced structure toppling.

Even long floating objects with uniform cross section that can effectively be treated as two-dimensional have proved to be quite rich in terms of stability classification. The circular cross section case is a notable exception. As anyone who has watched professional lumberjack log-rolling competitions—or tried such a feat themselves—knows, there is no preferred stable orientation in terms of the log's two-dimensional circular cross section. Ulam posed the question as to whether there are long floating objects of uniform density with cross sections other than the circle that have no preferred stable orientation. Curiously, such objects —known as Ulam shapes—do exist. Understanding and classifying such objects continues to attract much interest (see [6–9]). Of additional note, Ryabod [10] very recently showed a higher-dimensional version of an Ulam shape: a set of fully three-dimensional convex shapes which are not balls but still float stably in every position.

The case of a long object with square cross section and uniform density is an excellent example of a floating shape with a non-trivial but analytically tractable stability picture. The stable floating orientations of this shape were first computed by Reid [11] to reveal that depending on the density ratio, ρ_{obj}/ρ_{fluid}, an entire family of orientations, including 'flat side up', 'corner up', and, notably, *any* orientation in between those could be observed. This situation was explored very recently by Feigel and Fuzailov [12] with both an elegant theoretical derivation and an accompanying set of table-top experiments that demonstrated precisely these novel predictions for the floating square. A number of other, mostly theoretical, studies have considered other shapes such as rectangles [13], equilateral triangles [14], as well as some three-dimensional shapes such as a cube, an octahedron, and a tetrahedron [15].

Our group has recently explored the case of the floating square with the possibility of an offset center of gravity as well as more general cases of two-dimensional shapes with any

---

[1] It is worth noting that for complex fluids, the precise details of the fluid mixture and its density require careful attention in the context of Archimedes' Principle (Physics Today, September 2012, Mark Wilson) [4].

specified polygonal cross section [16]. We included with these predictions results from an experimental study in which we floated 3D printed shapes matching the shapes studied theoretically. We used a potential energy formulation, based on ideas in Gilbert [8], to identify stable orientations. In one series of experiments, we floated 3D printed shapes with a square cross section and a hole along the long axis into which we could insert a nail. We observed both theoretically and experimentally that the stability predictions in terms of orientation angle versus density ratio evolved away from the predictions for the uniform square (e.g. Reid [11], Feigel and Fuzailov [12]) when the center of gravity was offset, breaking the four-fold symmetry of the floating square. In addition to these studies we 3D-printed more complex shapes, and showed how the experimentally observed stable floating orientations compared with our theoretical predictions.

There has been considerable interest and attention paid to the problem of floating objects and surface tension effects. Keller [17] characterized the equilibrium force balance and identified the modifications to the classical buoyant force on the object. This work provides an elegant reinterpretation of Archimedes' Principle when surface tension forces are present. Floating objects subject to buoyant and surface tension forces have been the subject of a recent review (Vella [18]) and have been studied for various geometries including, for example, long floating cylinders of circular cross section (Lee and Kim [19], Naylor and Tsai [20]), circular, triangular, and hexagonal cross sections (Liu *et al* [21]), as well as arbitrary cross sections (Zhang *et al* [22]).

The problem of multiple floating objects and surface tension effects has also attracted significant attention. As anyone who has observed their floating cold cereal in a bowl may have noted, this is a nontrivial problem even for spherical objects (e.g. Vella and Mahadevan [23]). Some of these studies have incorporated the influence of a nonzero density in the upper fluid or even continuous density stratification (e.g. Vella and coworkers [18, 24, 25], Lee [26], Magnaudet and Mercier [27], and Cooray *et al* [28]). When dynamics of falling objects are the focus, effects related to impact and entrainment of the upper fluid also come into play (e.g. Magnaudet and Mercier [27], Li *et al* [29], and McLaughlin and coworkers [30–32]). Dynamics associated with imbalances in horizontal forces are also quite fascinating. Such studies include the work of Burton *et al* [33] and Janssens *et al* [34, 35] who have explored horizontal propulsion of an object due to Marangoni forces, which have many applications, including biolocomotion [36].

In the present paper we focus exclusively on fluid statics and do not incorporate surface tension into our models. Our theory, which incorporates the two-fluid form of Archimedes' Principle, departs from previous studies by carefully reexamining the potential energy argument of Gilbert [8] to update this for the two-fluid (two-density) problem. We demonstrate the connection of this potential energy formulation to that of the single-fluid setting. In the appendix, we show an *N*-fluid extension of this argument, but we focus our experiments only on single- and two-fluid configurations. In this work, we have the following objectives:

- We extend arguments for floating objects at an air–fluid interface (i.e. with density of air neglected) to the case of floating objects at the interface between two fluids, each of nonzero density. Our theory will show how the two-fluid case can be effectively mapped back to the single-fluid case. We explore this also experimentally with different one- and two-fluid combinations including water, mineral oil (less dense than water), and corn syrup (more dense than water). Figure 1 shows examples of three different objects under consideration floating at an oil–water interface.
- We use long shapes with uniform cross section, but allow any cross-sectional shape that can be approximated by a polygon. We then use 3D printing to generate these nontrivial
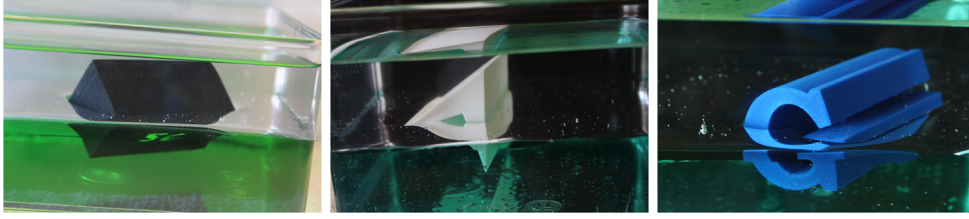
Figure 1. Long uniform density objects with fixed cross sections floating at an oil–water interface. From left to right: the Square, the Arrow, and the Letter G.

shapes to float and compare the observations to our predictions. We provide descriptions and publicly-available code [37] so that interested readers with access to 3D printing and Matlab may explore their own related studies. We point out successes and challenges associated with floating these objects in single- and two-fluid systems.

- We additionally explore stability predictions by varying the density of the object for a given shape (experimentally by controlling the 3D printed 'infill' settings) as well as by floating the same object in fluids of different densities. In doing so, we shall demonstrate an example of what we refer to as 'density-induced tipping' where we observe experimentally the catastrophic-type orientation transitions as the density of the fluid is slowly altered.

The paper is organized as follows. In section 2 we give definitions and theoretical results. In order to make sure the discussion is self-contained, section 2.1 contains a set of physical definitions and concepts. We then give needed modifications to apply these ideas to the two-fluid interface in section 2.2. In section 3, we describe the methodology of our numerical and experimental work. In section 3.1 we explain how the theory is implemented computationally for the prediction of stable floating configuration for long objects with an arbitrary cross section. Section 3.2 describes methods for design and 3D printing of floating objects. Section 4 gives the results of our floating experiments with water, syrup, oil, and combinations therein, comparing and contrasting them with the theory. In particular, we have done experiments using a variety of density ratios for three different cross sections: a square in section 4.1, an arrow in section 4.2, and a letter G in section 4.3. In section 4.4, we describe the effects of time variation and present density induced tipping. In section 5 we give conclusions and future plans.

2. Theoretical results

Here we review basic definitions and concepts associated with static floating objects including center of gravity, center of buoyancy, and Archimedes' Principle. Specifically we address how these, along with a definition of potential energy, are framed in the two-fluid context.

2.1. Archimedes' Principle and other physical concepts

Consider an object described by a continuous density function $\rho_{\mathrm{obj}}(x, y, z)$ within a domain $\Omega_3 \in \mathbb{R}^3$. The mass of the object is given by

$$M_{\mathrm{obj}} = \iiint_{\Omega_3} \rho_{\mathrm{obj}}(x, y, z) \, \mathrm{d}V.$$

If the object has a fixed cross section Ω and length L with density independent of z, then

$$\Omega_3 = \Omega \times [0, L], \; \rho_{\text{obj}}(x, y, z) = \rho_{\text{obj}}(x, y), \text{ and} M_{\text{obj}} = L \iint_\Omega \rho_{\text{obj}}(x, y) \, dA.$$

If the object additionally has uniform density (i.e. ρ_{obj} is constant) and its fixed cross sectional area is A_{obj} then

$$M_{\text{obj}} = \rho_{\text{obj}} A_{\text{obj}} L. \tag{1}$$

Definition 1 (**Center of Gravity, Centroid**). The center of gravity, which is the balance point of the object, is given by

$$\langle G_x, G_y, G_z \rangle = \frac{1}{M_{\text{obj}}} \iiint_{\Omega_3} \langle x, y, z \rangle \, \rho_{\text{obj}}(x, y, z) \, dV. \tag{2}$$

For a fixed cross section object of length L with density independent of z, this becomes

$$\vec{G} = \langle G_x, G_y \rangle = \frac{L}{M_{\text{obj}}} \iint_\Omega \langle x, y \rangle \, \rho_{\text{obj}}(x, y) \, dA, \text{ and} G_z = \frac{L}{2}. \tag{3}$$

If the object has uniform density, then the center of gravity coincides with the *centroid*.

Definition 2 (**Center of buoyancy**). The center of buoyancy of an object submerged in a single fluid of constant density ($\rho_{\text{f}}(x, y, z) = $ constant) is the center of gravity of the fluid that has been displaced by the object, i.e. the centroid of the submerged domain. If the submerged domain Ω_{sub} has volume V_{sub} then

$$\langle B_x, B_y, B_z \rangle = \frac{1}{M_{\text{f}}} \iiint_{\Omega_{\text{sub}}} \langle x, y, z \rangle \, \rho_{\text{f}}(x, y, z) \, dV = \frac{1}{V_{\text{sub}}} \iiint_{\Omega_{\text{sub}}} \langle x, y, z \rangle \, dV, \tag{4}$$

where $M_{\text{f}} = \rho_{\text{f}} V_{\text{sub}}$ is the mass of the displaced fluid. As with the center of gravity, for an object of length L with fixed cross section, $B_z = \frac{L}{2}$, and $\vec{B} = \langle B_x, B_y \rangle$ can be computed with a double integral.

As noted earlier, we will generally be working with long objects whose cross sections are polygons. This significantly simplifies the computations of quantities such as $\vec{G}$ and $\vec{B}$. To establish the notation we will use, a cross section Ω is a polygon with vertices

$$\{(x_1, y_1), (x_2, y_2), ..., (x_N, y_N), (x_1, y_1)\}, \tag{5}$$

given in *counterclockwise orientation*. For such a polygon, the area and center of gravity have closed form expressions given by

$$A_{\text{obj}} = \frac{1}{2} \sum_{k=1}^N (x_k + x_{k+1})(y_{k+1} - y_k),$$

and

$$G_x = \frac{1}{6 A_{\text{obj}}} \sum_{k=1}^N (x_k^2 + x_k x_{k+1} + x_{k+1}^2)(y_{k+1} - y_k),$$

$$G_y = \frac{-1}{6 A_{\text{obj}}} \sum_{k=1}^N (y_k^2 + y_k y_{k+1} + y_{k+1}^2)(x_{k+1} - x_k). \tag{6}$$

For the proof of these statements, see [16]. Given a location of the waterline, $y = h$, the cross section of the submerged portion of the object is also a polygon (since the waterline is a straight line) whose area, $A_{\text{sub}}(h)$, is a function of h. Therefore, the center of buoyancy $\vec{B}$ can also be calculated using equations like equation (6) once the submerged points are identified.

Principle 2.1 (**Archimedes**). The upward buoyant force exerted on an object wholly or partially submerged is equal to the weight of the displaced fluid. Note that the displaced fluid can be a single fluid of constant density, two fluids each with their own density, or a fluid with continuous density stratification. See Keller [17] for a reinterpretation of this when surface tension is present and the waterline is not flat. In the present work we neglect surface tension effects, and so in the case of a single constant density fluid, Archimedes' Principle can be expressed as

$$M_{\text{obj}}g = \rho_{\text{f}} V_{\text{sub}} g,$$

where g is acceleration due to gravity, ρ_{f} is the density of the fluid, and V_{sub} is the volume of the submerged portion of the object. The quantity $\rho_{\text{f}} V_{\text{sub}} g$ is exactly the vertical component of the force that arises due to the hydrostatic pressure integrated over the fluid–solid interface. For an object of uniform density ρ_{obj} and uniform cross section this implies

$$R = \frac{\rho_{\text{obj}}}{\rho_{\text{f}}} = \frac{V_{\text{sub}}}{V_{\text{obj}}} = \frac{A_{\text{sub}}(h_0)}{A_{\text{obj}}}. \tag{7}$$

We refer to R as the *density ratio* of the object. This equation shows that Archimedes' Principle determines the height of the waterline, $y = h_0$, of an object at equilibrium with no other external forces.

For density ratio $0 < R < 1$, equation (7) implies that h_0 is determined by $W(h_0) = 0$ where W given by

$$W(h) = R - \frac{A_{\text{sub}}(h)}{A_{\text{obj}}}.$$

Note that W is a continuous function of h. If h is sufficiently small, the object lies entirely above the water, $A_{\text{sub}}(h) = 0$, and $W(h) > 0$. If h is sufficiently large, $A_{\text{sub}}(h) = A_{\text{obj}}$, and $W(h) = R - 1 < 0$. By the Intermediate Value Theorem, this implies that for some h between these two values Archimedes' Principle is satisfied, i.e. $W(h = h_0) = 0$. For any $0 < R < 1$, the object floats partially submerged at the air–fluid interface. From a computational point of view, for a polygonal shape $W(h)$ can be evaluated using only vertices of the polygon (and the submerged portion thereof) and the waterline height h_0 can be obtained by solving a root-finding problem. For the results reported in this paper we have used the bisection method for solving this root-finding problem.

Archimedes' Principle can be satisfied for any rotation of an object, but this, by itself, does not establish stability of a given equilibrium floating configuration. To address stability, we will establish a potential energy for each fixed orientation of the object, such that the local minima of this energy give the object's stable floating configurations. To do so, it is convenient to work in a reference frame where the object is fixed and the waterline moves. In particular, given an angle θ, let $\hat{n}(\theta)$ be the unit normal vector orthogonal to the waterline. In the reference frame fixed to the object, the center of gravity is independent of θ and R, whereas the center of buoyancy varies with both θ and R. The stable floating configurations for a single-fluid case (e.g. air density equals zero) can be determined by finding the minima of the following potential energy function $U(\theta, R)$, previously described in [8] and used in [14, 16].
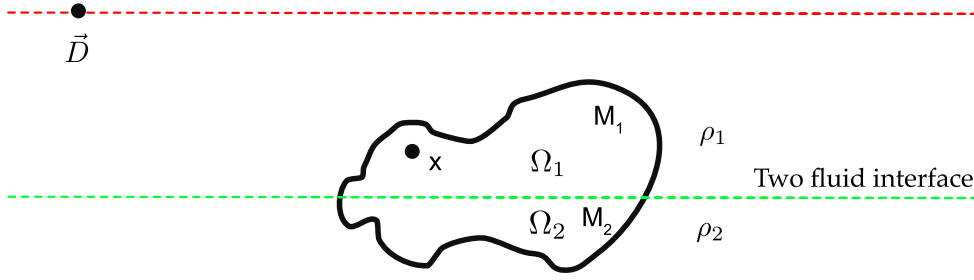
Figure 2. A schematic diagram of the two-fluid problem. Fluid 1 has density ρ_1, and fluid 2 has density ρ_2, and the green dashed line is the two-fluid interface. The object's cross section consists of two pieces: Ω_1, displacing fluid 1, and Ω_2 displacing fluid 2. M_1 and M_2 are the corresponding masses of the displaced fluids. Point $\vec{D}$ is an arbitrary point on the air–fluid interface. We assume the object lies completely below the red dashed line, the top of fluid 1.

Definition 3 (**Potential energy**). At equilibrium, the (scalar) potential energy of a floating object is given by

$$U(\theta, R) = M_{\text{obj}}g\,\hat{n}(\theta) \cdot (\vec{G} - \vec{B}(\theta, R)), \tag{8}$$

where '·' indicates a dot product. See Gilbert [8]. Given R and waterline orientation θ we can determine the submerged region Ω_{sub} and its area A_{sub} consistent with Archimedes' Principle, and thus $\vec{B}(\theta, R)$. Then, equation (8) establishes the potential energy $U(\theta, R)$ as a continuous function of θ and R.

2.2. Floating objects at the two-fluid interface

The previous discussion, particularly the details of the potential energy formulation, describes an object floating partially submerged in a single fluid, where the upper fluid (e.g. air) has negligible density. In this section, we extend the classical concepts to objects floating at the interface between two fluids of different density. We show that the two-fluid case fits neatly into the previous single-fluid framework, with a reinterpretation of the density ratio R and the potential energy function. The two-fluid problem can be stated as follows.

Question 2.1 (**Two-fluid problem**). Given an object fully submerged in fluid 1 and partially submerged in fluid 2 (see figure 2); how can we determine its stable floating orientations?

Here we restrict ourselves to the case of a uniform density object with fixed cross section. Consider the situation shown in figure 2. In particular, for an object of constant density ρ_{obj} floating at the interface between two fluids with densities ρ_1 and ρ_2, we have

$$\rho_1 < \rho_{\text{obj}} < \rho_2.$$

Let $\Omega = \Omega_1 \cup \Omega_2$ where Ω_1 is the cross section of the object contained in fluid 1, with area A_1, and Ω_2 the cross section in fluid 2 with area A_2. Thus

$$A_{\text{obj}} = A_1 + A_2 \quad \text{and} \quad V_{\text{obj}} = (A_1 + A_2)L = A_{\text{obj}}L. \tag{9}$$

Let $M_1 = \rho_1 A_1 L$ and $M_2 = \rho_2 A_2 L$ denote the masses of the displaced fluids.

We can rewrite the center of gravity from equation (3) as

$$\vec{G} = \frac{L}{M_{\text{obj}}}\left(\iint_{\Omega_1} \langle x, y \rangle \, \rho_{\text{obj}} \, dA + \iint_{\Omega_2} \langle x, y \rangle \, \rho_{\text{obj}} \, dA\right),$$

$$= \frac{1}{A_{\text{obj}}}\left(\iint_{\Omega_1} \langle x, y \rangle \, dA + \iint_{\Omega_2} \langle x, y \rangle \, dA\right). \tag{10}$$

Definition 4 (**Centroids of** Ω_1, Ω_2). Let $\vec{B}_1$ be the centroid for Ω_1 and $\vec{B}_2$ be the centroid for Ω_2. That is,

$$\vec{B}_1 = \frac{1}{A_1} \iint_{\Omega_1} \langle x, y \rangle \, dA \text{ and } \vec{B}_2 = \frac{1}{A_2} \iint_{\Omega_2} \langle x, y \rangle \, dA. \tag{11}$$

Since both fluids have constant density these can be rewritten as

$$\vec{B}_1 = \frac{L}{M_1} \iint_{\Omega_1} \langle x, y \rangle \, \rho_1 \, dA \text{ and } \vec{B}_2 = \frac{L}{M_2} \iint_{\Omega_2} \langle x, y \rangle \, \rho_2 \, dA. \tag{12}$$

From equations (10) and (11) one can deduce that

$$\vec{G} = \frac{1}{A_{\text{obj}}}(A_1\vec{B}_1 + A_2\vec{B}_2) = \vec{B}_2 + \frac{A_1}{A_{\text{obj}}}(\vec{B}_1 - \vec{B}_2). \tag{13}$$

Definition 5 (**Center of buoyancy for the two-fluid interface**). Using the notation above, the center of buoyancy of the object at the two-fluid interface can be written as

$$\vec{B} = \frac{L}{M_1 + M_2} \iint_{\Omega_{\text{obj}}} \langle x, y \rangle \, \rho_{\text{f}}(x, y) \, dA, \text{ where } \rho_{\text{f}}(x, y) = \begin{cases} \rho_1 & \text{if } (x, y) \in \Omega_1 \\ \rho_2 & \text{if } (x, y) \in \Omega_2 \end{cases}.$$

Using equation (12) we can write $\vec{B}$ as:

$$\vec{B} = \frac{1}{M_1 + M_2}(M_1\vec{B}_1 + M_2\vec{B}_2) = \vec{B}_2 + \frac{M_1}{M_1 + M_2}(\vec{B}_1 - \vec{B}_2). \tag{14}$$

Note that from equations (13) and (14) the center of gravity $\vec{G}$ and the center of buoyancy $\vec{B}$ are both on the line segment connecting the centroids $\vec{B}_1$ and $\vec{B}_2$. Further, since $\rho_1 < \rho_2$,

$$\frac{M_1}{M_1 + M_2} = \frac{\rho_1 A_1}{\rho_1 A_1 + \rho_2 A_2} < \frac{A_1}{A_1 + A_2} = \frac{A_1}{A_{\text{obj}}}.$$

It follows that $\vec{B}$ is closer to $\vec{B}_2$ than $\vec{G}$ is. That is, in terms of their vertical components, $\vec{B}$ is always lower than $\vec{G}$ for an object with uniform density.
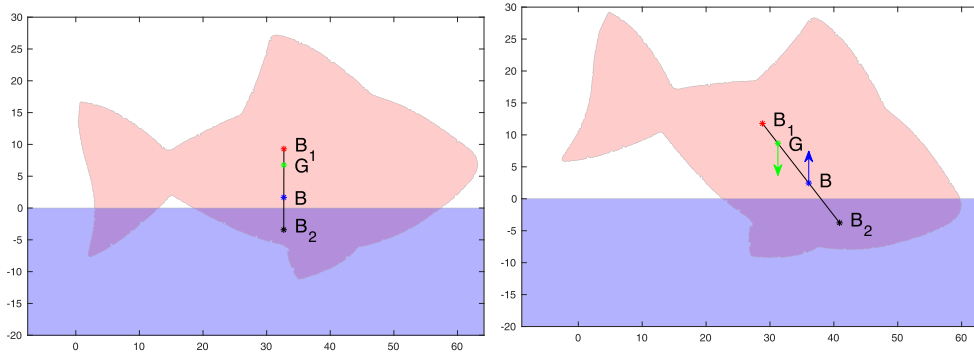
Archimedes' Principle says that in the absence of other forces (e.g. surface tension), the balance of forces when the object is at equilibrium requires $M_1 g + M_2 g = M_{\text{obj}} g$. That is,

$$M_1 + M_2 = M_{\text{obj}}. \tag{15}$$

In terms of densities and areas this can be written as

$$\rho_1 A_1 + \rho_2 A_2 = \rho_{\text{obj}} A_{\text{obj}}. \tag{16}$$

Together, equations (9) and (16) give a system of equations for A_1 and A_2 which can be solved to get

Figure 3. An object floating at a two-fluid interface: on the left, the object is in a stable floating configuration, where $\vec{B}_2$, $\vec{B}$, $\vec{G}$, and $\vec{B}_1$ align vertically. On the right, the object is in an unstable position, where the four points are still collinear, but the line is not vertical. In this figure on the right, the arrows indicate the downward gravitational force at $\vec{G}$ and the upward buoyant force at $\vec{B}$; these forces would cause the object to rotate counterclockwise. In these examples we have used $\tilde{R} = (\rho_{\mathrm{obj}} - \rho_1)/(\rho_2 - \rho_1) = 0.2$ and $\rho_1/\rho_{\mathrm{obj}} = 0.5$ (note this means $\rho_2/\rho_{\mathrm{obj}} = 3$).

$$A_1 = A_{\mathrm{obj}} \frac{\rho_2 - \rho_{\mathrm{obj}}}{\rho_2 - \rho_1} \quad \text{and} \quad A_2 = A_{\mathrm{obj}} \frac{\rho_{\mathrm{obj}} - \rho_1}{\rho_2 - \rho_1}. \tag{17}$$

In view of equation (16), note that equation (14) becomes

$$\vec{B} = \vec{B}_2 + \frac{\rho_1}{\rho_{\mathrm{obj}}} \frac{A_1}{A_{\mathrm{obj}}} (\vec{B}_1 - \vec{B}_2). \tag{18}$$

Comparing this with equation (13) shows that the exact position of $\vec{B}$ is between $\vec{G}$ and $\vec{B}_2$. Figure 3 shows two examples of the four points $\vec{B}_2$, $\vec{B}$, $\vec{G}$, and $\vec{B}_1$; under the conditions stated so far, these four points are always collinear. We give further interpretations of this figure below, as our discussion so far does not address stability of configurations satisfying Archimedes' Principle. First, we make one more important observation.

Combining equations (13) and (18) allows us to eliminate $\vec{B}_1$ to find that

$$\vec{G} - \vec{B} = k(\vec{G} - \vec{B}_2), \tag{19}$$

where k is a θ-independent constant given by

$$k = 1 - \frac{\rho_1}{\rho_{\mathrm{obj}}}.$$

The subtle, and perhaps unremarkable, result in equation (19) turns out to plays a key role in the potential energy formulation for the two-fluid system. In particular, the following theorem extends the potential energy in definition 3 to the two-fluid system and at the same time provides an elegant mapping back to the single-fluid system.

Theorem 2.1 (**Potential energy in the two-fluid interface**)**.** *Using the notation established in this section, there exists a constant* k *independent of the orientation of the object, and a suitably-defined density ratio* $\tilde{R}$ *such that*

$$U(\theta, \tilde{R}) = M_{\mathrm{obj}} g \hat{n} \cdot (\vec{G} - \vec{B}) = k M_{\mathrm{obj}} g \hat{n} \cdot (\vec{G} - \vec{B}_2(\theta, \tilde{R})), \tag{20}$$

under the conditions established by Archimedes' Principle, $M_1 + M_2 = M_{\mathrm{obj}}$.

Before giving the proof of this result, we pause to give insight for what it provides. For a fixed object, we determine the value of the density ratio $\tilde{R}$, and for this value of $\tilde{R}$ we consider U as a function of θ only. The θ values for which the potential energy has local minima correspond to stable floating configurations for this object. For this fixed $\tilde{R}$ case, the Archimedes' Principle is a significant constraint on the locations of $\vec{G}$ and $\vec{B}$ relative to centroids $\vec{B}_1$ and $\vec{B}_2$. In particular, as long as $0 < \tilde{R} < 1$ these two vectors, along with $\vec{B}_1$ and $\vec{B}_2$ will always be distinct and collinear with their vertical components arranged in the order $\vec{B}_2$, $\vec{B}$, $\vec{G}$, $\vec{B}_1$. If $\tilde{R} \leqslant 0$ or $\tilde{R} \geqslant 1$, then the object is fully submerged in a single fluid, and we are no longer in the two-fluid case. Figure 3 shows two example configurations, one stable (on the left) and one unstable (on the right). In the stable configuration on the left the four points are vertically-aligned. In the configuration on the right, although the object is in a position where Archimedes' Principle is satisfied, the non-vertical alignment of $\vec{G}$ and $\vec{B}$ would cause the object to rotate in the counter-clockwise direction.

The above paragraph discusses the four vectors $\vec{B}_2$, $\vec{B}$, $\vec{G}$, and $\vec{B}_1$, but we do not need to compute all of them in the search for potential energy minima. In the end, we only need $\vec{G}$ and $\vec{B}_2$. This follows from the result in equation (19) that the difference $\vec{G} - \vec{B}$ is proportional to the difference $\vec{G} - \vec{B}_2$ with the constant of proportionality $k = 1 - \rho_1/\rho_{\text{obj}}$. The first form of the potential energy in (20), involving directly the difference $\vec{G} - \vec{B}$, indicates that the two-fluid potential energy takes the same form as the single-fluid potential energy. In either situation, the essential physical quantities are the center of gravity and the center of buoyancy. The key difference, of course, is that to compute $\vec{B}$ for the two-fluid system one must account for the displacement of fluid 1 *and* fluid 2. The second form of the potential energy in (20), in contrast to the first form, involves directly the difference $\vec{G} - \vec{B}_2$ along with a constant k, which indicates that the two-fluid potential energy, like the single-fluid potential energy, can be computed in terms of the centroid of the displaced lower fluid (fluid 2). *In particular, one need not compute $\vec{B}_1$ (and one need not compute $\vec{B}$).* Now, recall that in the single-fluid case, the appropriate density ratio $\tilde{R}$ was $\rho_{\text{obj}}/\rho_{\text{f}}$. In the two-fluid configuration with two different densities ρ_1 and ρ_2 the relative density ratio $(\rho_{\text{obj}} - \rho_1)/(\rho_2 - \rho_1)$ has already made an appearance in Archimedes' Principle and is a leading candidate for $\tilde{R}$.[2] These together imply that in order to find stable floating configurations at the two-fluid interface, the calculation will be the same as in the single-fluid case, with one important caveat associated with the density ratio. Note that specification of the constant k requires a value of ρ_1/ρ_{obj}, however, while this scales the two-fluid potential energy the value of k does not modify in any way the configurations for which local minima of the potential energy are achieved. The proof of theorem 2.1 outlined below, which generalized the discussion of the potential energy in Gilbert [8], reveals the subtlety of how the relevant features of the potential energy needed to assess stability require only the relative density ratio $(\rho_{\text{obj}} - \rho_1)/(\rho_2 - \rho_1)$ and, critically, the displaced lower fluid.

Proof. The potential energy function is defined to be the sum of functions:

$$U(\theta) = U_G + U_B ,$$

where U_G is the potential energy due to gravity and the object's mass, and U_B is the potential energy due to buoyancy. First, the work done against gravity to lift the object relative to a reference point on the air–fluid interface, denoted by $\vec{D}$, is given by

---

[2] Spoiler Alert: see equation (26).

$$U_G = M_{\text{obj}} g \hat{n} \cdot (\vec{G} - \vec{D}), \tag{21}$$

where, as in the previous section, $\hat{n}$ represents a unit vector normal to the uppermost (air–fluid) interface, in this context in the opposite direction to the gravity vector—i.e. $\vec{g} = -g\hat{n}$. Next, we define U_B as the work required to lift displaced fluid from its original position in the submerged region to reference point $\vec{D}$. This is a general statement that would apply for fluid with variable density $\rho_{\text{f}}(x, y, z)$ with total fluid mass M_{f}. That is,

$$U_B = M_{\text{f}} g \hat{n} \cdot (\vec{D} - \vec{B}), \tag{22}$$

where $\vec{B}$ is the center of buoyancy associated with the displaced fluid computed using the variable density form in equation (4). Archimedes Principle requires that $M_{\text{f}} = M_1 + M_2 = M_{\text{obj}}$ so that

$$U_B = M_{\text{obj}} g \hat{n} \cdot (\vec{D} - \vec{B}). \tag{23}$$

Combining equations (21) and (23) gives the potential energy of the object. That is:

$$U(\theta) = M_{\text{obj}} g \hat{n} \cdot ((\vec{G} - \vec{D}) + (\vec{D} - \vec{B})) = M_{\text{obj}} g \hat{n} \cdot (\vec{G} - \vec{B}). \tag{24}$$

Combining this with equation (19) shows immediately that

$$U(\theta) = k M_{\text{obj}} g \hat{n} \cdot (\vec{G} - \vec{B}_2), \tag{25}$$

where $k = 1 - \rho_1/\rho_{\text{obj}}$ is independent of orientation and only depends on the density ratio ρ_1/ρ_{obj}.

In norder to complete the proof, we need to define the constant $\tilde{R}$. From equations (11) and (17), the term $M_{\text{obj}} \vec{B}_2 = L A_{\text{obj}} \vec{B}_2$ depends only on the ratio

$$\frac{A_2}{A_{\text{obj}}} = \frac{\rho_{\text{obj}} - \rho_1}{\rho_2 - \rho_1} := \tilde{R}, \tag{26}$$

which defines the relative density ratio $\tilde{R}$ given in the statement of the proof. □

We emphasize the takeaway message of this theorem: Although the primitive form of potential energy clearly involves the center of buoyancy, and hence contributions from the displaced fluids in region Ω_1 and Ω_2, an alternate form can be expressed in terms of the center of gravity and the centroid of the displaced fluid 2. Specifically, terms related to $\vec{B}_1$ do not appear. The potential energy identified in equation (25) has the same form as the single-fluid result in equation (8) if we write

$$U(\theta, \tilde{R}) = \tilde{M}_{\text{obj}} g \hat{n}(\theta) \cdot (\vec{G} - \tilde{\vec{B}}(\theta, \tilde{R}))$$

where $\tilde{M}_{\text{obj}} = k M_{\text{obj}} = M_{\text{obj}} - \rho_1 A_{\text{obj}}$ is the effective mass of the object already submerged in fluid 1, $\tilde{\vec{B}}(\theta, \tilde{R})$ is the center of buoyancy of the displaced *lower* fluid region Ω_2 whose area, A_2, satisfies $A_2/A_{\text{obj}} = \tilde{R}$ (Archimedes' Principle). This formulation recovers the standard single-fluid results when $\rho_1 = 0$ and $\tilde{R} = \rho_{\text{obj}}/\rho_2$.

To summarize, the two-fluid problem can be solved in exactly the same way as the single-fluid case with the caveat that the density ratio be interpreted as $\tilde{R} = (\rho_{\text{obj}} - \rho_1)/(\rho_2 - \rho_1)$. In the appendix, we show that for an object floating across three or more fluid layers, it is no longer possible to write $\vec{G} - \vec{B}$ in a way that depends only on a single displaced-fluid's centroid. That is, the general *N*-fluid case does not map directly back to the single-fluid case. In the next section, we will give more details of the logistics for the two-fluid predictions, and then describe how we create floating objects to test these predictions.
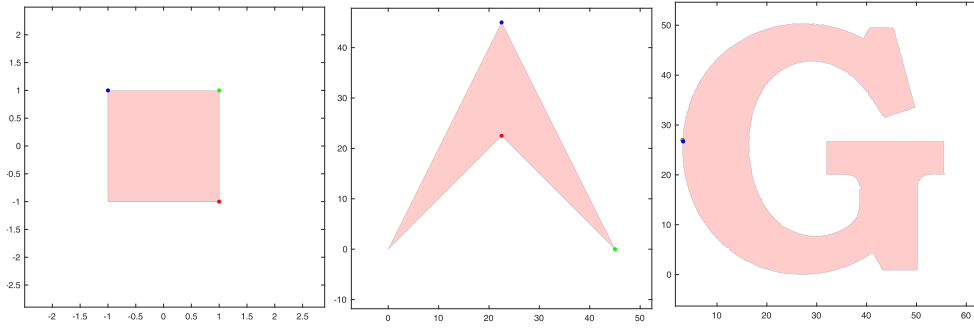
Figure 4. The Square, Arrow, and Letter G cross sections that we will use in our experiments. The orientations as shown in this figure correspond to $\theta = 0$. Positive (negative) θ corresponds to rotation of the object in the clockwise (counter-clockwise) direction.

3. Methods

In the previous section, we presented a theoretical framework by which one can identify the stable orientations of long objects with fixed cross section floating at the interface between two fluids. In section 3.1, we implement this theory numerically in order to predict stable floating configurations. In section 3.2, we describe the process of creating such objects using 3D printing and discuss practical details for testing the theory experimentally. The software used in this section is publicly available, cf. the Iceberg Project [37].[3] We hope to inspire others to try such floating experiments. The needed equipment and supplies are fairly modest.

3.1. Numerical methods for prediction

We now outline how to predict stable floating configurations for objects with fixed cross sections. All of the computations shown here have been performed using the `Matlab` code `PotentialEnergyFloat`, a portion of our Iceberg Project software [37].

Consider an object with a polygonal cross section, defined by counterclockwise-oriented vertices $\{(x_1, y_1), ..., (x_N, y_N), (x_1, y_1)\}$ as in equation (5). Our computations and experiments concentrate on three main shapes: the square, the arrow, and the letter G, as in figure 4. The first, second, and third points are depicted in red, green, and blue (indicating counterclockwise orientation). The first two of these shapes can be described quite simply by polygons. For example, the square is defined by vertices $\{(1, -1), (1, 1), (-1, 1), (-1, 1)\}$. The arrow is similarly given by four vertices (plus the repeated one). In contrast, the letter G is a much more complicated polygon involving 2106 vertices. However, there is no difference in either the theory or computation, except that the computations take longer.

Given a (polygonal) shape and a density ratio $R \in (0, 1)$ we can compute the potential energy landscape. Recall that the relevant two-fluid density ratio is given by $R = (\rho_{\text{obj}} - \rho_1)/(\rho_2 - \rho_1)$ (see equation (26)) which includes the single-fluid special case where $\rho_1 = 0$. Figure 5 shows the computed value of

$$\bar{U} = U/(\tilde{M}_{\text{obj}}g).$$

[3] A portion of the code was originally written for [16], but it has since been significantly expanded.
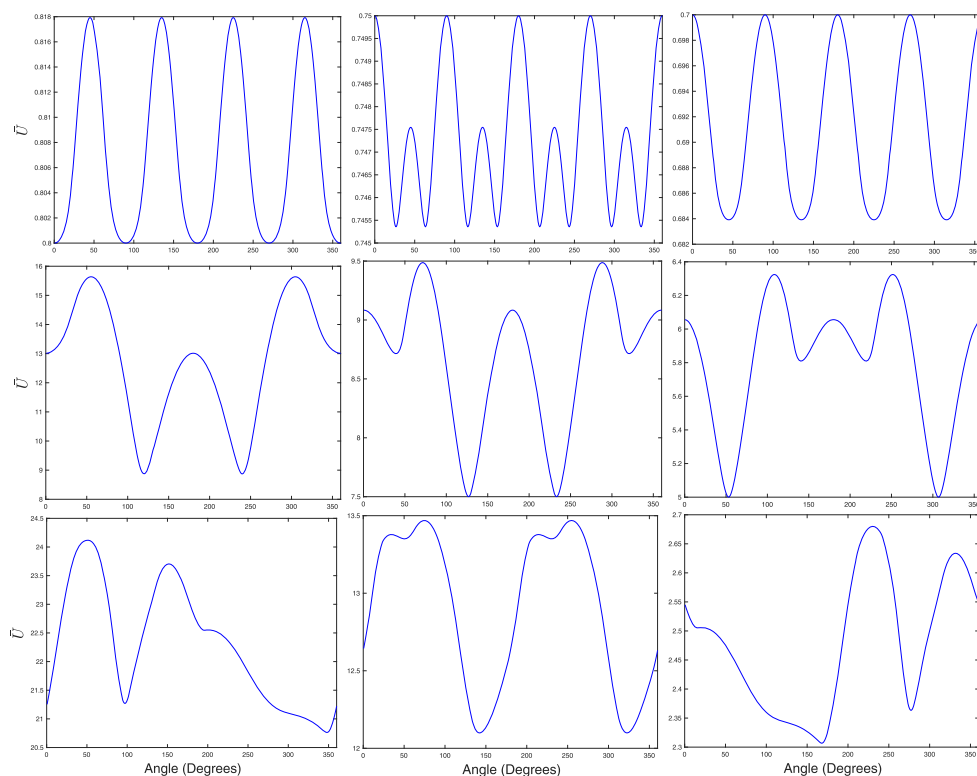
Figure 5. Potential energies $\bar{U}$ for different shapes and R values: top row: the square for $R = 0.2, 0.25, 0.3$. Middle row: the arrow for $R = 0.2, 0.4, 0.6$. Bottom row: the letter G for $R = 0.1, 0.5, 0.9$.

Since $\tilde{M}_{\mathrm{obj}}g$ is independent of θ, we can view this as equivalent to potential energy, in the sense that it has the same local minima, and therefore gives a measure of the stable configurations. The figure shows $\bar{U}$ as a function of the object orientation for the square (top row), the arrow (middle row) and the Letter G (bottom row) at various fixed values of R. The orientation angle θ represents the *clockwise orientation of the object* relative to the waterline with the reference configuration, $\theta = 0$, corresponding to the orientations shown in figure 4. Alternatively, one can view θ as a *counterclockwise orientation of the waterline* with the object fixed. In either view, the angles associated with the local minima of the potential energy correspond to stable floating configurations of the object, in the absence of surface tension and other external forces.

The top row of figure 5 shows the potential energy function $\bar{U}$ for the square for $R = 0.2$, 0.25, 0.3. In the $R = 0.2$ case, the square has four stable floating configurations, at angles $\theta = 0, 90, 180, 270$ degrees (i.e. flat side up). For $R = 0.25$, the square has eight stable floating configurations, and for $R = 0.3$, there are again four stable states, but this time with angles $\theta = 45, 135, 225, 315$ degrees (i.e. corner up). These stable configurations for the square have been studied previously by Reid [11] and by Feigel and Fuzailov [12] for the single-fluid context. We emphasize here that their theory applies also for the two-fluid cases but with R given by equation (26).

The second row of figure 5 shows the potential energy of the arrow for $R = 0.2, 0.4, 0.6$, corresponding to three, four, and four stable floating configurations, respectively. Since the
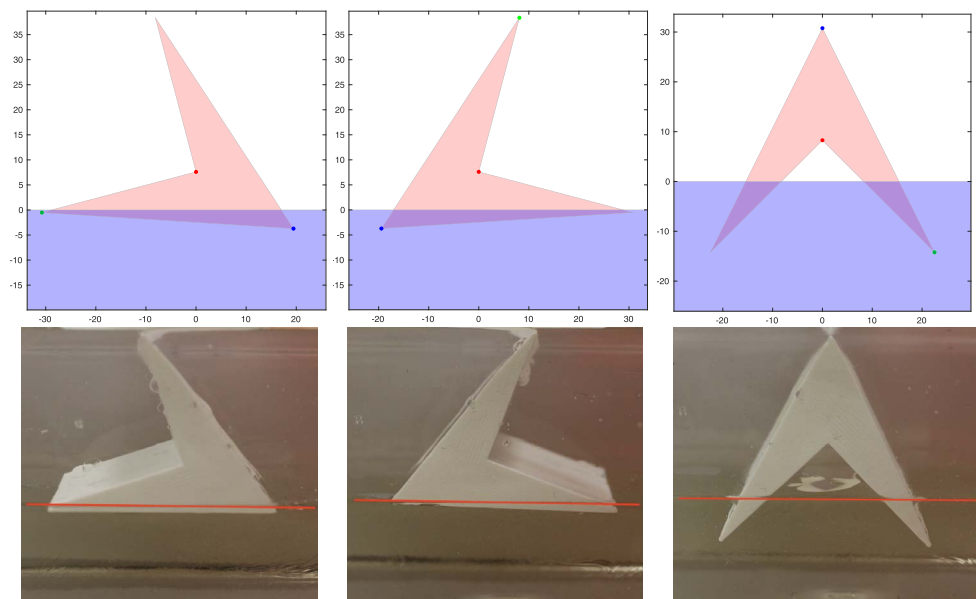
Figure 6. The top three plots show the predicted stable floating orientations of the arrow for $R = 0.2$. These are the orientations with $\theta = 120$, 240, 360 (aka 0) degrees respectively. The lower three photographs show the observed floating orientations for an arrow at an oil–syrup interface (red line) where the predicted density ratio is also 0.2.

potential energy at fixed R is a smooth function, we can use numerical minimization techniques in order to find the local minima—i.e. the stable floating orientations. The stable floating orientations of the arrow for $R = 0.2$ are (to the nearest degree) computed to be $\theta = 120$, 240, 360 (aka 0) degrees. These three stable configurations are depicted in figure 6 along with photographs of an arrow with $R = 0.2$ in oil (upper fluid) and syrup (lower fluid) showing experimental realizations of these stable floating configurations. We also list stable floating configurations for the other two R values depicted in figure 5 (middle row): for $R = 0.4$, $\theta = 39$, 127, 233, 321 degrees; and for $R = 0.6$, $\theta = 53$, 141, 219, 307 degrees.

All of the square and arrow stable configurations shown in figure 5 are quite pronounced, and we would not expect that small perturbations would affect them significantly. The third row of figure 5 shows the potential energy for the Letter G for $R = 0.1$, 0.5, 0.9. In contrast to the potential energy functions for the arrow and the square, there are stable configurations (local minima of the potential energy) for the letter G where small perturbations would be likely to destroy or significantly change its stability. For $R = 0.5$ there are four stable points at orientations $\theta = 51$, 143, 231, 323 degrees and, while all qualify as stable equilibria, the local potential energy well is not very deep at 51 and 231, and intuitively these would seem to be less stable than the two others at 143 and 323. At $R = 0.9$ there are three stable points at orientation $\theta = 16$, 168, 277 degrees. Although the value $R = 0.1$ looks like it would also have three stable points, there are only two stable points for $\theta = 97$ and 348 degrees. What about the point at $\theta = 195$ degrees? At a slightly smaller density ratio, $R = 0.09$, this is a stable point but, nearby, at $R = 0.1$, the point at $\theta = 195$ is no longer a local minimum. A bifurcation has occurred between these values. Even at $R = 0.09$, a floating object in this configuration could easily be perturbed by the slightest inconsistency in distribution of mass
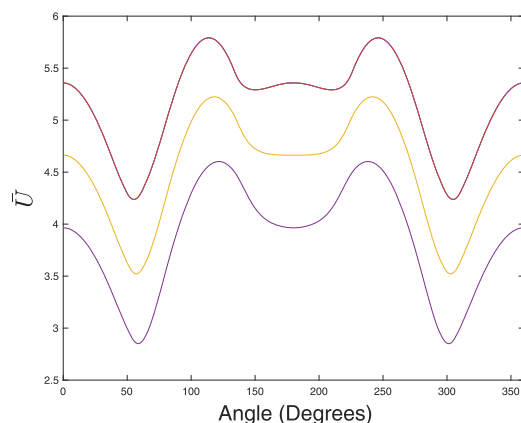
Figure 7. This graph shows the potential energy $\bar{U}$ for the arrow for $R = 0.65, 0.7, 0.75$. This shows the transition between four stable configurations (upper curve) and three stable configurations (lower curve). The middle curve occurs close to a bifurcation point, and for this R value it would be very hard to distinguish experimentally whether there are three or four stable configurations.

or any slight disturbance of the fluid(s). Therefore, in cases such as these for the Letter G, we would expect that these stable points may be hard to observe experimentally due to the natural fluctuations in mass distribution of the physical objects and in a floating tank of non-theoretical fluid.

Bifurcations do occur for the square and arrow cases as well. Figure 7 shows the potential energy of the arrow for three different values of R near 0.7. Here the local minima are so close to the tipping point that finding a third floating configuration would be extremely difficult and the theoretically-predicted stable configuration may disappear due to small fluctuations. This sensitivity is a general hallmark of behavior near bifurcation.

In order to get a more global picture of the stable floating orientations for all values of R, instead of only finding the stable orientations for a fixed value of R, we will compile these stable angles for all values of R in a θ versus R bifurcation diagram. We display such diagrams below for our experiments with these three shapes (the square, the arrow, and the letter G). We note that such figures contains a lot more information, but at the expense of being able to see information on whether the local minimum is at the onset of a bifurcation, and therefore susceptible to disappear due to fluctuations. In subsequent figures, we will plot such figures with angles measured in radians, and on the range $(-\pi, \pi)$. This change from degrees on $(0, 360)$ to this range can be accomplished using the following formula:

$$\theta_{\text{radian}} = \frac{\pi}{180} (\text{mod} (\theta_{\text{degree}} + 180, 360) - 180). \tag{27}$$

3.2. Experimental design

In order to test our theoretical predictions, we need a way to create a long object with the same fixed cross section that we have used for our numerical simulations. To this end, we have developed a method using Matlab and OpenSCAD for converting any digital image for a cross section into a 3D-printable object with this cross section cf the `DesignFloat` portion of the Iceberg Project package [37]. With a fully digital version of the cross section, we can
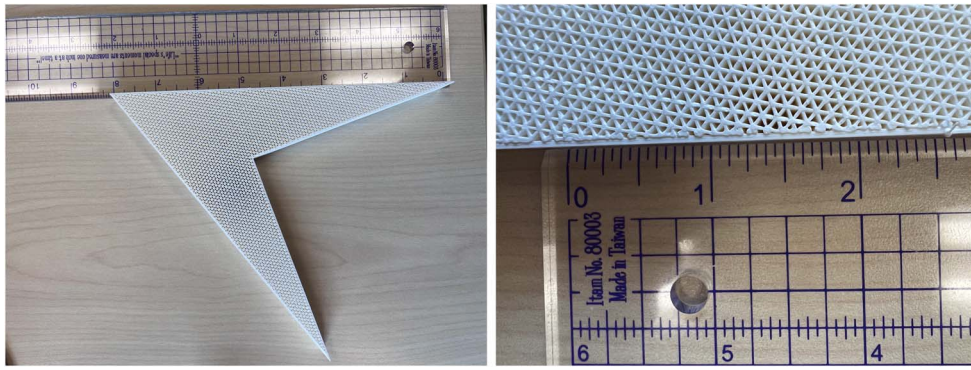
Figure 8. These images show a partially-printed large arrow with 80% infill. The ruler shows one inch markings.

compute the exact volume and the stable floating configurations for the particular object we have printed, even when the object has a complex cross section.

We print using PLA, a type of plastic which has a density heavier than water. However, we are able to modify the uniform density by adjusting the infill density of the print, thereby allowing us to create floating objects with the same shape and different densities over a wide variety of densities. Figure 8 shows an example of a partially printed large arrow with 80% infill density using the 'grid' infill pattern.[4] We can see that this print is very uniform throughout the object. For prints above about 20% infill, we previously found that a uniform density estimate is reasonable [16]. This citation also suggests how to estimate the density of the object prior to printing it. Once printed, we measured the mass of the object, and then established its (uniform) density ρ_{obj} by dividing the mass by the calculated volume. Based on this and the densities of water, syrup, and mineral oil[5] listed in table 1 we obtain the R values for all of our floating objects. Figure 9 shows our experimental set up with a small arrow floating at an oil–water interface.

4. Experimental results

Here we report various experimental results and comparisons with our theoretical predictions. In our experiments, we used objects with three different cross sectional shapes—square, arrow, and letter G—as shown in figure 4. The squares all had the same dimensions but with different infills to control ρ_{obj} (see table 1). We used arrows and Letter G shapes with both large and small cross section and a variety of infills (see table 1). An example of a partially-printed large cross section arrow is shown in figure 8. The squares and small cross section objects were all designed to be 'long' in the third dimension. The large cross section objects were relatively short in the third direction (approximately 1 inch) but when these objects were floated, we gently constrained the object so that its axis in the third dimension remained parallel with the fluid–fluid interface (as if it were a long object).

Although our theory can be applied to predict stable orientations for long objects with any cross section, experiments with such objects are not without some difficulties that are worth

---

[4] Other infill patterns would work as well, but we recommend using a 2D infill pattern rather than a 3D infill pattern in order to keep a fixed cross section.
[5] We used Bluewater Chemgroup mineral oil and Karo light corn syrup with real vanilla.

Table 1. Density, mass, and volume measurements for the fluids and 3D printed objects. Multiple measurements of the oil and syrup densities gave error estimates for these quantities. We used PLA density measurement estimates from [16]. For each shape the multiple mass measurements correspond to different objects; for example, we used six different square cross-section objects. Uncertainties in the masses are based on multiple measurements on different scales. Volume uncertainties are based on dimension uncertainties for each object.

Description	Parameter	Value
Density	ρ_{PLA}	1.15 ± 0.02 g cm^{-3}
	ρ_{water}	1.0 g cm^{-3}
	ρ_{oil}	0.83 ± 0.01 g cm^{-3}
	ρ_{syrup}	1.36 ± 0.03 g cm^{-3}
Square	M_{square}	[11.45; 19.18; 50.34; 50.92; 51.56; 55.69] ± 0.3 g
(3 cm $\times$ 3 cm $\times$ 6 cm)	V_{square}	54 ± 1 cm^3
Arrow (Small)	$M_{smallarrow}$	[26.8; 27.42; 32.06; 43.08] ± 0.1 g
	$V_{smallarrow}$	[33.9; 33.9; 33.9; 44.5] ± 0.5 cm^3
Arrow (Big)	$M_{bigarrow}$	[180.6; 180.8] ± 1 g
	$V_{bigarrow}$	200.74 ± 5 cm^3
Letter G (Small)	M_{smallG}	[15.03; 39.9; 36.03] ± 0.1 g
	V_{smallG}	40.2 ± 1 cm^3
Letter G (Big)	M_{bigG}	[332.7; 455.5] ± 1 g
	V_{bigG}	561.4 ± 10 cm^3

pointing out. As noted above, our model does not account for surface tension effects. The Bond number, $Bo = (\rho_2 - \rho_1)g\ell^2/\gamma$ where ℓ is a representative length scale for our objects and γ is the relevant fluid–fluid surface tension, measures the buoyant force relative to surface tension forces. For air–water $\gamma = 72 \times 10^{-3}$ N m^{-1} and $g \approx 10$ m s^{-2}. For an object with $\ell \approx 10^{-2}$ m (small objects) and $\ell \approx 10^{-1}$ m (large objects), the Bond number is $\mathcal{O}(10) - \mathcal{O}(1000)$. For the two-fluid systems under consideration the Bond numbers involves the density difference $\rho_2 - \rho_1$ which for all combinations we have considered is less than ρ_{water}. We feel our large cross section objects are relatively insensitive to surface tension effects. We anticipate that some of the discrepancies observed between our theory and experiments, especially for the smaller objects, may be attributed to surface tension.

Another issue we point out here and discuss more below, especially for the two-fluid configurations, is the effect of entrainment of one fluid in another fluid of different density. For example, when experimenting with an object floating at an oil–water interface the observed floating orientation can be sensitive to the way in which the object reaches the interface. If, for example, the oil–water layers are set up first and then the object is dropped through the oil to the oil–water interface an entrained layer of oil may surround the entire
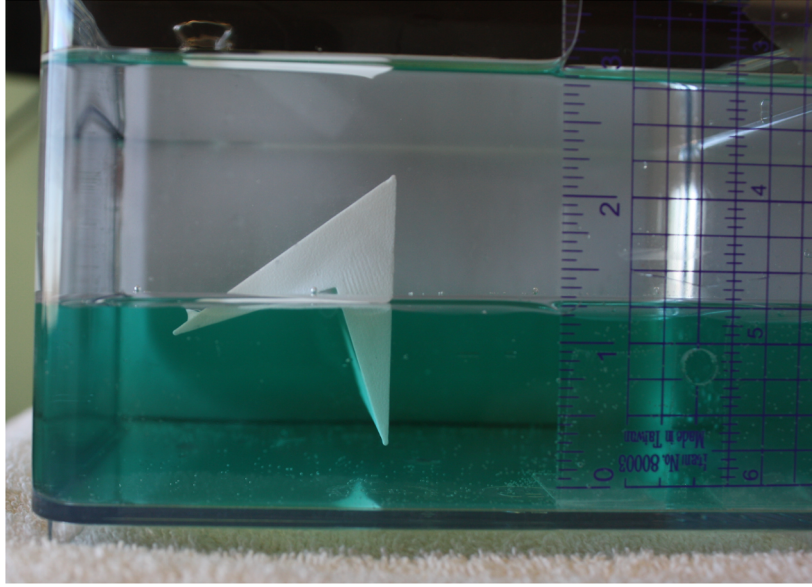
Figure 9. This image shows an example of our experimental set up used to float the smaller objects, here shown with an arrow at an oil–water interface with the lower fluid (water) dyed green. The ruler shows one inch markings.

object and modify its effective buoyancy at least over time scales for which the entrained oil drains off of the object (out of the water layer region). On the other hand, if the object is first floating at a air–water interface and oil is slowly filled to submerge the object the same entrainment of oil by the object does not occur but some entrainment of water into the oil may occur. We have typically used the former approach but have made tests using the latter approach. A few other experimental challenges are pointed out in the conclusion.

We explore two key aspects of the theory by floating a variety of 3D printed shapes and sizes in different fluid systems. The first prediction of the theory follows directly from Archimedes' Principle which relates the submerged (cross sectional) area A_2 to the known (cross sectional) area of the object and the appropriate object and fluid densities. To test this prediction in our experiments we define the experimentally-observed density ratio

$$R_{\mathrm{obs}} = \frac{A_2^{\mathrm{obs}}}{A_{\mathrm{obj}}^{\mathrm{obs}}}, \tag{28}$$

where A_2^{obs} is the experimentally-observed area below the fluid–fluid interface and $A_{\mathrm{obj}}^{\mathrm{obs}}$ is the experimentally-observed total area of the object. Both of these areas are measurable from photographs taken during the experiments. To be precise, A_2^{obs} is taken to be the area of the object below a straight line connecting two far-field points on the fluid–fluid interface. We can then compare this *observed density ratio* with the *expected density ratio* $R = (\rho_{\mathrm{obj}} - \rho_1)/(\rho_2 - \rho_1)$ where the object and fluid densities are measured independently. The second prediction of the theory involves the stable floating orientation(s) for a given density ratio. These predicted orientations are the minima of the potential energy landscapes for each fixed R, as outlined earlier. Since the theoretically-predicted stable orientations depend on the density ratio, we compare our experimentally-observed floating orientations to these theoretical predictions with both the *observed* R_{obs} and *expected* R values in mind.
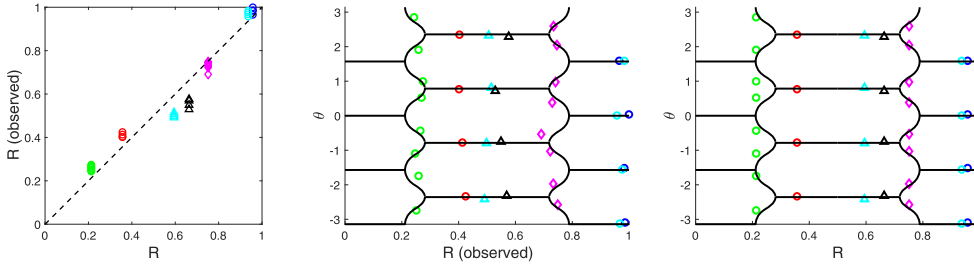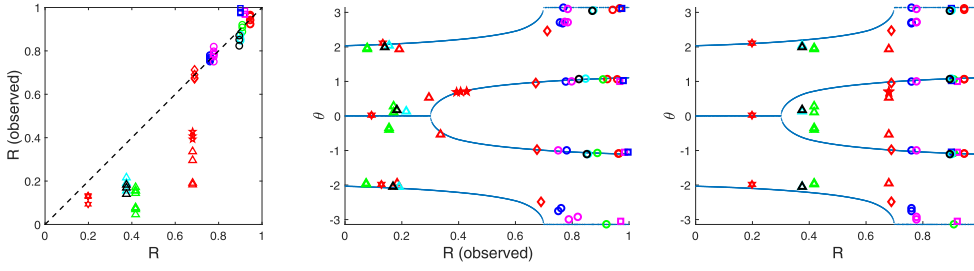
Figure 10. Square: the left plot shows the observed density ratio versus the expected density ratio. Experimental observations are indicated by symbols ('∘' = air–water, '◇' = air–syrup, '△' = oil–water). Each different color corresponds to one of six different squares. In the middle plot, experimental data are plotted using R_{obs}. In the right plot, experimental data are plotted using R.

4.1. The square cross section

We first examine objects with square cross sections (i.e. 'squares'). As noted earlier, this case has been examined by a number of authors and most recently by Feigel and Fuzailov [12]. Feigel and Fuzailov derived theoretical results for the stable orientations as a function of the density ratio R and explored these experimentally for a range of density ratios near $R = 0.25$. As we have argued, the theory applies not only for squares floating at an air–fluid interface but also for squares at a two-fluid interface. As a demonstration of this we show several experimental measurements in figure 10 for squares floating in various single fluids (water, oil, syrup) as well as at a two-fluid interface (e.g. oil–water).

The plot on the left of figure 10 shows the experimentally-observed density ratio R_{obs} versus the expected density ratio. Six different squares were used, each corresponding to different colored markers in the plot (see also table 1). We report R_{obs} for each observed stable orientation; for example, four slightly different values of R_{obs} are shown by the black '△' corresponding to four observed stable floating orientations of that object in the oil–water system. Note that the cyan '△' (with $R \approx 0.6$, oil–water interface) and the cyan '∘' (near $R \approx 0.94$, air–water interface) represent the same physical object. These data generally show that these objects float with close to the expected submerged area of the lower fluid; a minor exception for the square is the oil–water system (see the data denoted by cyan and black '△').

The middle plot of figure 10 compares the observed stable floating orientations at the observed density ratio ('∘' = air–water, '◇' = air–syrup, '△' = oil–water; see also table 2) versus the theoretical predictions for these square objects. The right plot of figure 10 shows the same results except that the observed angles are plotted at the theoretically-expected density ratio. The solid curves in these plots correspond to the theoretical prediction of Feigel and Fuzailov [12] given by their equations (5) and (16), symmetrically and periodically extended to cover the full range of angles $[-\pi, \pi]$. We show this full range in order to assess the symmetry of the experimentally-observed floating orientations in comparison to the theoretical symmetry of the square. That is, we report all observed floating orientations on $[-\pi, \pi]$, which in some cases is four and others eight consistent with the theory. We have also confirmed that our general-purpose code predictions for squares agrees with the Feigel and Fuzailov theory. While most of these experimental data correspond to different square objects, note that the case of the cyan '△' (near $R \approx 0.6$, oil–water interface) and the cyan '∘' (near $R \approx 0.94$, air–water interface) represent the same physical object. This confirms experimentally a key message that the same object floating at an air–water interface can have a different equilibrium floating configuration at an oil–water interface.

Figure 11. Arrow: the left plot shows the observed density ratio versus the expected density ratio. Experimental observations are indicated by symbols ('o' = air–water, '□' = air–oil, '◇' = air–syrup, '△' = oil–water, '✡' = oil–syrup, '⋆' = oil–water/ modified filling). Each different color corresponds to one of six different arrows. In the middle plot, experimental data are plotted using R_{obs}. In the right plot, experimental data are plotted using R. Note that the oil–syrup example (✡) corresponds to the three experimental images in figure 6.

Table 2. Symbols for the experimental data for different fluid–fluid systems. Note that in the first three, the first 'fluid' is air, corresponding to the one layer cases. The case listed as 'oil–water (mod)' uses a modified protocol in which the object is first floated at the air–water interface and oil is poured carefully onto the water surface to minimize/ eliminate possible entrainment of oil by the object that occurs in our standard protocol for the oil–water system.

o	Air–water
□	Air–oil
◇	Air–syrup
△	Oil–water
▽	Water–syrup
✡	Oil–syrup
⋆	Oil–water (mod)

4.2. The arrow cross section

We next examine objects with arrow-shaped cross sections (referred to below as 'arrows'). This shape has not been explored previously and so we have used our general purpose code to obtain theoretical predictions for stable floating orientations as a function of density ratio.

The plot on the left of figure 11 shows the experimentally-observed density ratio R_{obs} versus the expected density ratio, R. Six different arrows were used (four smaller arrows— red, green, blue, magenta—and two larger arrows—cyan and black) and multiples of these were floated in different fluid–fluid systems (see tables 1 and 2). We see that the arrows with relatively large density ratio (e.g. 0.8 or higher) seem to have observed density ratios close to the expected density ratios. Data for the oil–water system (denoted by symbol '△') have observed density ratios that are considerably smaller than the expected density ratio. We discuss this observation further below. The middle plot of figure 11 compares the observed stable floating orientations at the observed density ratio. The right plot of figure 11 shows the same results except that the observed angles are plotted at the theoretically-expected density

ratio. The solid curves in these plots correspond to the theoretical prediction from our general purpose code.

As is clear in the left plot of R_{obs} versus R, in some of these cases (notably the oil–water system marked by '$\triangle$' and '$\star$') there is a significant difference between the observed and expected density ratio. We mention two possible explanations for these observations: (A) surface tension may play a significant role in providing a non-negligible vertical force that effectively 'lifts' the object higher than expected, (B) entrainment of the upper (oil) occurs when the object is submerged through the oil to the oil–water interface and this entrained oil fully or partially coats the object and provides a measure of additional buoyancy not accounted for in our model. The estimated Bond number suggests that surface tension could play a role for the smaller arrows but likely not for the larger arrows. We do observe that the agreement between observed and theoretically-expected density ratio is better with the larger arrows (the black and cyan '$\triangle$') compared to the small arrows (the red and green '$\triangle$').

To investigate the influence of entrainment of the oil, we repeated one of the experiments using a modified tank-filling protocol. We first note that our standard protocol for floating an object at an oil–water interface is to set up the oil–water layers first and then drop the object in though the oil and let it settle on the oil–water interface. As is know for related experiments studying effects of entrainment for falling beads (e.g. see McLaughlin and coworkers [30–32]), as the object falls through the oil and reaches the underlying water layer, it carries with it an effective personal floatation device in the form of a relatively buoyant layer of oil as it descends into the water layer. Eventually, this oil layer will drain upwards back to the upper oil region but the time scale for this to occur we believe is longer than the time we have waited to make observations. In the modified protocol, we float the object *first* at an air–water interface and then carefully add an oil layer so that at least the portion of the object already in the water does not have a coating of oil. These experiments are shown by the symbol '$\star$'. These do show an observed density ratio closer to the expected density ratio. That said, there is still a discrepancy which could be explained in part by (A). We further comment that while this may be a better experimental protocol for the oil–water system it is also much more difficult and time consuming to collect data as measurement of each orientation of each object would require draining and refilling the oil layer. An alternative approach is to allow a much longer time to elapse before making a measurement so that any entrained oil drains from the water portion. However, the time scale for the entrained oil to drain off the object is probably quite long.[6]

In terms of the stable orientations, these are shown in the middle and right plots of figure 11. The best comparisons occur in the middle plot when the experimentally-observed angles are plotted against the experimentally-observed density ratio. This provides the best test of the stable angle prediction in the sense that we use a density ratio known to be consistent with the experiments and Archimedes' Principle. We observe that the best comparisons are for the largest density ratios (heaviest objects) and for regions of the bifurcation diagram away from the transition points near density ratios of 0.3 and 0.7.

---

[6] A balance of viscous forces and gravity forces suggests $\mu V/\ell^2 \sim \Delta\rho g$ where μ is the fluid viscosity, V is a draining velocity scale, ℓ is a length scale, and $\Delta\rho$ is the density difference (e.g. $\rho_{water} - \rho_{oil}$). If we identify a time scale T required for draining using $V \sim \ell/T$ then $T \sim \mu/(\Delta\rho g\ell)$. For water the viscosity is $\mu \sim 10^{-3}$ Pa s and for mineral oil the literature suggests a viscosity 10–100 times greater. For a length scale $\ell \sim 10^{-2}$ m this gives $T \sim 10$ s for air–water but maybe a 100–1000 times longer for oil–water since not only is the oil viscosity larger but the density difference, $\rho_{water} - \rho_{oil}$, is smaller.
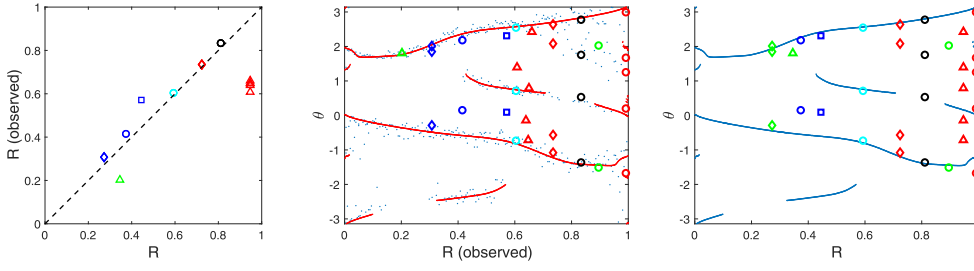
Figure 12. Letter G: the left plot shows the observed density ratio versus the expected density ratio. Experimental observations are indicated by symbols ('○' = air–water, '□' = air–oil, '◇' = air–syrup, '△' = oil–water). The different colors correspond to different arrows used experimentally; we floated five different Letter G's (three smaller ones—red, green, blue—and two larger ones—cyan and black) and multiples of these were floated in different fluid–fluid systems. In the middle plot, experimental data are plotted using R_{obs}. Here the red curves corresponds to the computed theoretical prediction while the scattered blue dots correspond to theoretically-predicted stable floating configurations when the center of gravity is perturbed using a random perturbation of 1% the size of the object. In the right plot, experimental data are plotted using R with the blue curves the same as the red curves in the middle plot. Note that there are a few experiments with R near 1 for which we were not able to extract observed density ratios.

4.3. The letter G cross section

We have previously shown that for a square with an offset center of gravity [16] the four-fold symmetry is broken and, for these off-center squares, the stable orientation branches can become discontinuous (e.g. see figure 13 in [16]). The letter G, which we explore next, also has discontinuous branches in the stable floating orientation as a function of density ratio even in the uniform density case.

The plot on the left of figure 12 shows the experimentally-observed density ratio R_{obs} versus the expected density ratio. Five different letter G's (three smaller ones—red, green, blue—and two larger ones—cyan and black) and multiples of these were floated in different fluid–fluid systems (see also table 1). The R_{obs} versus R are in good agreement with the exception, again, of the oil–water system (the red and green '△').

There appears to be reasonable agreement between some of the experimentally-observed orientations and the theoretically-predicted ones for the Letter G, as can be seen in middle/ right plots of figure 12. These tend to occur along the two continuous solution branches that extend across the full range of density ratios. There also appear to be regions in parameter space, especially for larger R and angles roughly in the $[0, \pi]$ range where experimentally-observed orientations do not appear to match the theory. Roughly these correspond to orientations in which the 'round' part of the letter G is above water. In some sense, the more the cross section resembles a circle, the more ambiguous will be the preferred floating orientations.[7] Two cases of note are the large letter G's plotted in cyan and black, both with the '○' symbol (air–water interface). The cyan '○' near $R = 0.6$ show excellent agreement with the predicted orientations. The black circles near $R = 0.83$ are in excellent agreement for the highest and lowest angles. However, two intermediate solutions are also observed when the theory formally predicts that they should not be observed. A closer inspection of the

---

[7] Log-rolling on a letter G is probably only slightly easier than on a proper log.
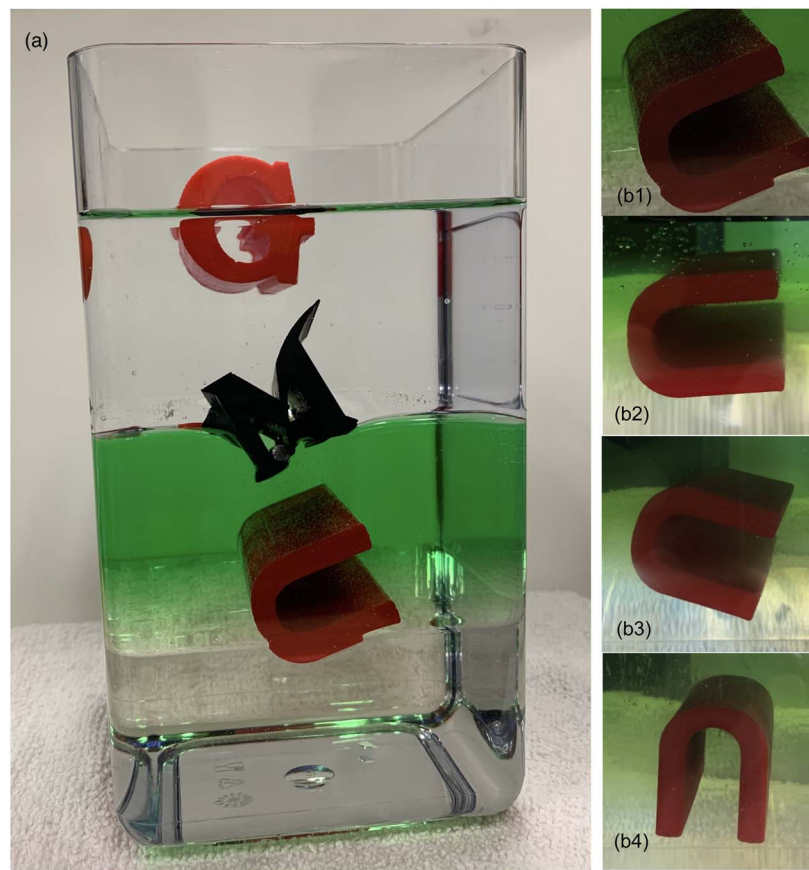
Figure 13. (a) The three fluids case of oil, water (colored green), and syrup on day 0. (b) Over time, the water and syrup diffused, resulting in a diffuse interface region and a syrup-water mixture, causing the U to rotate clockwise. (b1) Taken from the left figure on day 0, (b2) day 8; (b3) day 15, (b4) day 56 (note: the U is still well away from the bottom of the tank).

theory, however, when a small change is made in the center of gravity of the object shows that there appear to be many nearly-stable solutions in this region. In particular, the middle plot of figure 12 shows the theoretical prediction as the red curves along with a large collection of blue points computed by allowing a small random perturbation (1% the size of the object) of the object's center of gravity. The results of this plot demonstrate that throughout the region between the two main red curves, especially for larger density ratios, there are nearby solutions if one allows even a small perturbation of the center of gravity. We think that potential energy landscape of the letter G has, in many instances (as demonstrated by the noisy set of equilibria), only weak departures from uniformity in θ. Surface tension is expected to be a small effect especially for these large Letter G shapes, however, it may still impact experimental observations in cases such as these that are only weakly stable and/or where there appear to be nearby stable solutions.

4.4. Time variation and density-induced tipping

In this section, we give a short discussion of two specific cases of tipping due to time variation in the study of floating objects. In fact, there are many other mechanisms in which one may observe tipping transitions. We will address these further in future work. Figure 13(a) shows a case of floating multiple objects at three different two-fluid interfaces in a tank layered with three fluids: syrup as the bottom layer, water (dyed green) in the middle, and oil as the top layer.[8] The letter G floats at an air–oil interface, the letter M at the oil–water interface, and the letter U at the water–syrup interface. We left this container sitting for several weeks (56 d) and, over that time period, we observed that the letter U rotated from slightly tipped (2 o'clock position) to all the way upside down (6 o'clock position), see figures 13(b1)–(b4). A cloudiness in the water–syrup interface is also visible in these images. That is, the syrup and water mixed via diffusion, and therefore the effective fluid density has changed. This mixture is no longer a two-fluid interface, since it now contains a murky intermediate layer in which the fluid density varies continuously between ρ_1 and ρ_2. In order to understand this 'density-induced tipping', a new model for floating in the murky, continuously varying density, layer is required. We do not know if the Letter U would have continued to rotate after day 56, as the experiment had to be halted when the syrup started to mold.

In another case of time variation, we also observed that the letter M on day 0 appeared to be floating very high on the water with notable oil–water interface deflection. Its configuration on day 56 (image not included) showed it considerably deeper in the water with an almost perfectly flat oil–water interface suggesting that the initial interface deflection is perhaps related to entrainment of the oil as the Letter M was dropped through the oil layer (and the oil's slow escape from the interstices of the M over hours/days). As previously mentioned, this may also be related to the fact that in our arrow and letter G experiments, the observations and measurements for the oil–water system appeared to be the ones furthest from theoretical predictions.

5. Conclusions

In this work, we have extended the ideas of Archimedes' Principle and of [16] and [8] to create a model for identifying the stable floating configurations of a 3D-printed object with uniform cross section at a two-fluid interface. As was done for the single-fluid case, we found the potential energy as a function of orientation and density ratio. A key result we showed here is that one can use the same potential energy formula for both single- and two-fluid cases with a simple reinterpretation of how the density ratio, *R*, is calculated. In particular, a useful result is that the two-fluid potential energy can be written in terms of the displaced lower fluid —the direct calculation of the displaced upper fluid is not required. Using this two-fluid potential energy and Archimedes' Principle, we identified the minima of these potential energy functions which correspond to the stable floating configurations for the object. In the appendix, we extended some of these ideas to the *N*-fluid configuration and showed that this more complicated setup does not map directly back to the single-fluid problem as does the two-fluid system.

We also developed a set of programs that input a 2D digital image of a cross section and produce a set of points from which a 3D printable object with the input shape can be created.

---

[8] Note that this is not the multiple fluid layer scenario described in the appendix as each object here is in contact with at most two fluids.

This workflow enables not only the numerical prediction of stable floating orientations for these objects but also the creation, via 3D printing, of physical objects of the exact same shape that can be floated. In the present study we explored shapes with square cross section, an arrow-shaped cross section, and a cross section of the Letter G.

As a final note, we point out that turning theoretical models into physical experiments always comes with a fair share of issues (or maybe more optimistically, opportunities). Some of these we have already mentioned, such as surface tension, the entrainment of oil in the oil–water system, and fluid–fluid diffusion over long time scales. Here we touch on a few other experimental challenges that we encountered. First of all, working with syrup is extremely slow, sticky, difficult, and messy.[9] Oil is slightly better. For objects in water, it was relatively easy to explore different floating orientations (for example the 8 stable equilibria in some cases for the square) as the object could be readily rotated and, if necessary, dabbed quickly with a towel to remove a center-of-gravity-changing puddle on the exposed part of the object. However, syrup easily coats the objects and it was simply not possible to rotate the object to a new configuration as the syrup coating would add significant mass, completely changing the object's stable floating configuration. This issue necessitated tedious washing, rinsing, and drying steps to prepare the object for another float. We encountered other difficulties with the large prints. First, due to size limitations of the printer, it was not possible to print the new objects with a correspondingly long cross section. Instead, we printed them relatively short in the third dimension, and created a cage-like structure to hold the print in a fixed, upright, floating position lengthwise. Second, we found that the larger size prints had small inconsistencies and were in some cases no longer watertight, even over the rather short time scales of our experiments. We found that the water-repellant coating Rustoleum, as was used by [20] in their experiments with wooden objects, did not work well with the PLA plastic of our prints. In the end, we used a polyurethane spray on varnish[10] which we found to be quite effective in keeping water out. This was confirmed by measuring the object's mass before and after the floating experiments.

Despite these challenges, we have demonstrated in our work that it is possible to print and float physical objects with essentially unlimited two-dimensional cross-sectional shapes, at single- and two-fluid interfaces and, using Archimedes' Principle and an accompanying potential energy function, to predict these observations.

Acknowledgments

---

[9] The phrase 'slow as molasses' comes to mind.
[10] Minwax Fast Drying Polyurethane Spray.

Data availability statement

Appendix. The *N*-fluid interface

A natural extension of the two-fluid case is an object with constant density, ρ_{obj}, floating across $N \geqslant 2$ fluid layers. In this situation, N horizontal fluid layers with densities $0 \leqslant \rho_1 < \rho_2 < \ldots < \rho_N$ each with its own prescribed layer thickness are arranged (for example in a tank). We assume the lowest layer, with largest density ρ_N, is sufficiently deep so that the lowest part of the object is not in contact with the bottom of tank. We allow for the possibility that the upper layer has zero density (e.g. as one might assume for air). We assume that $0 < \rho_{\mathrm{obj}} < \rho_N$ so that the object does not sink through all the layers. Unless otherwise indicated, there are no further assumptions about the relation between ρ_{obj} and the other fluid layer densities. Below we outline equilibrium conditions required for this situation and comment on the special cases with $N = 2$ and $N = 3$ layers.

   The first two requirements are that the object is completely submerged in these N layers and that Archimedes' Principle applies. For a sufficiently long object with uniform cross sectional area A_{obj}, these conditions are stated as

$$A_{\mathrm{obj}} = \sum_{i=1}^{N} A_i, \qquad \rho_{\mathrm{obj}} A_{\mathrm{obj}} = \sum_{i=1}^{N} \rho_i A_i, \tag{29}$$

where ρ_i is the density of fluid i and A_i is the area of displaced fluid i.

   We have already argued in the main text that the potential energy associated with a static floating object in a fluid of any density stratification is

$$U = M_{\mathrm{obj}} g \hat{n} \cdot (\vec{G} - \vec{B}), \tag{30}$$

where $\hat{n}$ is the upward unit normal to the uppermost interface, $\vec{G}$ is the (2D) center of gravity of the object and $\vec{B}$ is the (2D) center of buoyancy of the displaced fluid, computed using a nonconstant fluid density.

   The center of gravity and the center of buoyancy formulas for the N-fluid situation are

$$A_{\mathrm{obj}} \vec{G} = \sum_{i=1}^{N} A_i \vec{B}_i, \tag{31}$$

$$\rho_{\mathrm{obj}} A_{\mathrm{obj}} \vec{B} = \sum_{i=1}^{N} \rho_i A_i \vec{B}_i, \tag{32}$$

where

$$\vec{B}_i = \frac{1}{A_i} \iint_{\Omega_i} \langle x, y \rangle \, \mathrm{d}A,$$

is the centroid of the displaced fluid of layer *i*. Then, observe that

$$
\begin{aligned}
\vec{G} - \vec{B} &= \sum_{i=1}^{N} \frac{A_i}{A_{\text{obj}}} \vec{B}_i - \sum_{i=1}^{N} \frac{\rho_i A_i}{\rho_{\text{obj}} A_{\text{obj}}} \vec{B}_i, \\
&= \sum_{i=1}^{N} \left(1 - \frac{\rho_i}{\rho_{\text{obj}}} \right) \frac{A_i}{A_{\text{obj}}} \vec{B}_i, \\
&= \left(1 - \frac{\rho_1}{\rho_{\text{obj}}} \right) \frac{A_1}{A_{\text{obj}}} \vec{B}_1 + \sum_{i=2}^{N} \left(1 - \frac{\rho_i}{\rho_{\text{obj}}} \right) \frac{A_i}{A_{\text{obj}}} \vec{B}_i.
\end{aligned}
\tag{33}
$$

From equation (31) observe that

$$
\vec{G} = \frac{A_1}{A_{\text{obj}}} \vec{B}_1 + \sum_{i=2}^{N} \frac{A_i}{A_{\text{obj}}} \vec{B}_i,
\tag{34}
$$

Using (34) to eliminate $\vec{B}_1$ from equation (33), assuming that $\rho_{\text{obj}} \neq \rho_1$, reveals

$$
\begin{aligned}
\vec{G} - \vec{B} &= \left(1 - \frac{\rho_1}{\rho_{\text{obj}}} \right) \left(\vec{G} - \sum_{i=2}^{N} \frac{A_i}{A_{\text{obj}}} \vec{B}_i \right) + \sum_{i=2}^{N} \left(1 - \frac{\rho_i}{\rho_{\text{obj}}} \right) \frac{A_i}{A_{\text{obj}}} \vec{B}_i, \\
&= \left(1 - \frac{\rho_1}{\rho_{\text{obj}}} \right) \vec{G} - \left(1 - \frac{\rho_1}{\rho_{\text{obj}}} \right) \sum_{i=2}^{N} \frac{A_i}{A_{\text{obj}}} \vec{B}_i + \sum_{i=2}^{N} \left(1 - \frac{\rho_i}{\rho_{\text{obj}}} \right) \frac{A_i}{A_{\text{obj}}} \vec{B}_i, \\
&= \left(1 - \frac{\rho_1}{\rho_{\text{obj}}} \right) \vec{G} - \sum_{i=2}^{N} \left(\frac{\rho_i - \rho_1}{\rho_{\text{obj}}} \right) \frac{A_i}{A_{\text{obj}}} \vec{B}_i, \\
&= \left(1 - \frac{\rho_1}{\rho_{\text{obj}}} \right) \left[\vec{G} - \sum_{i=2}^{N} \left(\frac{\rho_i - \rho_1}{\rho_{\text{obj}} - \rho_1} \right) \frac{A_i}{A_{\text{obj}}} \vec{B}_i \right].
\end{aligned}
\tag{35}
$$

To interpret the summation in this expression, we define the center of buoyancy associated with displaced fluid in layers 2 through *N* as $\vec{\mathcal{B}}$ with densities measured relative to the density of fluid layer 1. That is

$$
\left(\sum_{i=2}^{N} (\rho_i - \rho_1) A_i \right) \vec{\mathcal{B}} = \sum_{i=2}^{N} (\rho_i - \rho_1) A_i \vec{B}_i.
\tag{36}
$$

Further, by eliminating A_1 from Archimedes' Principle in (29) we find that

$$
\begin{aligned}
\rho_{\text{obj}} A_{\text{obj}} &= \rho_1 A_1 + \sum_{i=2}^{N} \rho_i A_i, \\
&= \rho_1 \left(A_{\text{obj}} - \sum_{i=2}^{N} A_i \right) + \sum_{i=2}^{N} \rho_i A_i, \text{ and thus}
\end{aligned}
$$

$$
(\rho_{\text{obj}} - \rho_1) A_{\text{obj}} = \sum_{i=2}^{N} (\rho_i - \rho_1) A_i.
\tag{37}
$$

It follows that

$$\vec{\mathcal{B}} = \sum_{i=2}^{N} \frac{(\rho_i - \rho_1)A_i}{(\rho_{\text{obj}} - \rho_1)A_{\text{obj}}} \vec{B}_i. \tag{38}$$

Therefore, using equation (35) the potential energy associated with the N-fluid system, assuming the case $\rho_{\text{obj}} \neq \rho_1$, can be written as

$$U = \left(1 - \frac{\rho_1}{\rho_{\text{obj}}}\right) M_{\text{obj}} g \hat{n} \cdot (\vec{G} - \vec{\mathcal{B}}), \tag{39}$$

where $\vec{\mathcal{B}}$ is given by equation (38).

Note that for the $N = 2$ case discussed in the main text

$$\vec{\mathcal{B}} = \frac{(\rho_2 - \rho_1)A_2}{(\rho_{\text{obj}} - \rho_1)A_{\text{obj}}} \vec{B}_2 = \vec{B}_2, \tag{40}$$

since Archimedes' Principle in that case implies $\rho_{\text{obj}}A_{\text{obj}} = \rho_1 A_1 + \rho_2 A_2 = \rho_1(A_{\text{obj}} - A_2) + \rho_2 A_2$. That is, in this case $\vec{\mathcal{B}}$ is simply the centroid, $\vec{B}_2$, of the displaced fluid 2.

However, for an object floating across three fluids, $N = 3$, we have

$$\vec{\mathcal{B}} = \frac{(\rho_2 - \rho_1)A_2}{(\rho_{\text{obj}} - \rho_1)A_{\text{obj}}} \vec{B}_2 + \frac{(\rho_3 - \rho_1)A_3}{(\rho_{\text{obj}} - \rho_1)A_{\text{obj}}} \vec{B}_3, \tag{41}$$

which, in general, is not the centroid of the region displaced by fluid 2 and fluid 3. That is, knowledge of the centroid of the displaced fluid 2 and 3 regions does not, by itself, provide enough information to determine the form of the potential energy. In the $N = 3$ case with air, oil, and water layers two experimental scenarios would be readily accessible: (A) $\rho_{\text{air}} < \rho_{\text{oil}} < \rho_{\text{obj}} < \rho_{\text{water}}$, or (B) $\rho_{\text{air}} < \rho_{\text{obj}} < \rho_{\text{oil}} < \rho_{\text{water}}$. The first case could be achieved by floating the object initially at an air–water interface, slowing adding an oil layer on the water layer until, eventually, the object would be floating submerged at a two-fluid oil–water interface. The second scenario can be similarly achieved except that since $\rho_{\text{obj}} < \rho_{\text{oil}}$, eventually, as the oil layer thickness becomes sufficiently large, the object would be raised out of the water and float at the air–oil interface. The intermediate scenarios in either cases (A) or (B) in which the object floats across the air–oil–water system would have a potential energy function that, in general, depends on the thickness of the intervening oil layer.

ORCID iDs

Daniel M Anderson ⬤ https://orcid.org/0000-0002-4923-2510
Evelyn Sander ⬤ https://orcid.org/0000-0003-4478-3919

References

[1] NIST 2016 Liquid density, (https://nist.gov/laboratories/tools-instruments/liquid-density)
[2] Curran J M, Hicks T N and Buckleton J S 2000 *Forensic Interpretation of Glass Evidence* (CRC Press/Taylor & Francis)
[3] FBI 2005 Glass density determination, (https://archives.fbi.gov/archives/about-us/lab/forensic-science-communications/fsc/jan2005/standards/2005standards8.htm)
[4] Wilson R M 2012 Custom shapes from swell gels *Phys. Today* **65** 15–6
[5] Rorres C 2004 Completing Book II of Archimedes's on floating bodies *Math. Intell.* **26** 32–42

[6] Auerbach H 1938 Sur un probleme de M. Ulam concernant l'equilibre des corps flottant *Studia Math.* **7** 121–42

[7] Florentin D, Schütt C, Werner E and Zhang N 2022 Convex floating bodies of equilibrium *Proc. Am. Math. Soc.* **150** 3037–48

[8] Gilbert E N 1991 How things float *Am. Math. Monthly* **98** 201–16

[9] Wegner F 2020 From elastica to floating bodies of equilibrium arXiv:1909.12596

[10] Ryabogin D 2022 A negative answer to Ulam's problem 19 from the Scottish Book *Ann. Math. (2)* **195** 1111–50

[11] Reid W P 1963 Floating of a long square bar *Am. J. Phys.* **31** 565–8

[12] Feigel Y and Fuzailov N 2021 Floating of a long square bar: experiment versus theory *Eur. J. Phys.* **42** 035011

[13] Delbourgo R 1987 The floating plank *Am. J. Phys.* **55** 799–802

[14] Erdös P, Schibler G and Herndon R C 1992 Floating equilibrium of symmetrical objects and the breaking of symmetry: I. Prisms *Am. J. Phys.* **60** 335–45

[15] Erdös P, Schibler G and Herndon R C 1992 Floating equilibrium of symmetrical objects and the breaking of symmetry: II. The cube, the octahedron, and the tetrahedron *Am. J. Phys.* **60** 345–56

[16] Anderson D M, Barreto-Rosa B G, Calvano J D, Nsair L and Sander E 2023 Mathematics of floating 3D printed objects *Proc. of Symposia in Applied Mathematics (PSAPM)* vol 79 ed M Trnkova and A Yarmola (American Mathematical Society) pp 19–50

[17] Keller J B 1998 Surface tension force on a partly submerged body *Phys. Fluids* **10** 3009–10

[18] Vella D 2015 Floating versus sinking *Annual Review of Fluid Mechanics* (*Annu. Rev. Fluid Mech.*) vol 47 (Annual Reviews) pp 115–35

[19] Lee D-G and Kim H-Y 2009 The role of superhydrophobicity in the adhesion of a floating cylinder *J. Fluid Mech.* **624** 23–32

[20] Naylor D and Tsai S S 2022 Archimedes' principle with surface tension effects in undergraduate fluid mechanics *Int. J. Mech. Eng. Educ.* **50** 749–63

[21] Liu J-L, Feng X-Q and Wang G-F 2007 Buoyant force and sinking conditions of a hydrophobic thin rod floating on water *Phys. Rev.* E **76** 066103

[22] Zhang F, Zhou X and Zhu C 2018 Effects of surface tension on a floating body in two dimensions *J. Fluid Mech.* **847** 489–519

[23] Vella D and Mahadevan L 2005 The Cheerios effect *Am. J. Phys.* **73** 817–25

[24] Vella D, Lee D-G and Kim H-Y 2006 The load supported by small floating objects *Langmuir* **22** 5979–81

[25] Vella D, Metcalfe P D and Whittaker R J 2006 Equilibrium conditions for the floating of multiple interfacial objects *J. Fluid Mech.* **549** 215–24

[26] Lee J 2018 The static profile for a floating particle *Colloids Interfaces* **2** 18

[27] Magnaudet J and Mercier M J 2020 Particles, drops, and bubbles moving across sharp interfaces and stratified layers *Annual Review of Fluid Mechanics* (*Annu.Rev. Fluid Mech.*) vol 52 (Annual Reviews) pp 61–91

[28] Cooray H, Cicuta P and Vella D 2017 Floating and sinking of a pair of spheres at a liquid-fluid interface *Langmuir* **33** 1427–36

[29] Li H, Chen H and Li E-Q 2022 Impact of superhydrophobic sphere onto a pool covered by oil layer *Phys. Fluids* **34** 03211

[30] Abaid N, Adalsteinsson D, Agyapong A and McLaughlin R 2004 An internal splash: levitation of falling spheres in stratified fluids *Phys. Fluids* **16** 1567–80

[31] Camassa R, Falcon C, Lin J, McLaughlin R and Mykins N 2010 A first-principle predictive theory for a sphere falling through sharply stratified fluid at low Reynolds number *J. Fluid Mech.* **664** 436–65

[32] Camassa R, Falcon C, Lin J, McLaughlin R and Parker R 2009 Prolonged residence times for particles settling through stratified miscible fluids in the Stokes regime *Phys. Fluids* **21** 031702

[33] Burton L, Chen N and Bush J 2014 The cocktail boat *Integr. Comp. Biol.* **54** 969–73

[34] Janssens S, Chaurasia V and Fried E 2017 Effect of a surface tension imbalance on a partly submerged cylinder *J. Fluid Mech.* **830** 369–86

[35] Janssens S, Koizumi S and Fried E 2017 Behavior of self-propelled acetone droplets in a Leidenfrost state on liquid substrates *Phys. Fluids* **29** 032103

[36] Bush J W and Hu D L 2006 Walking on water: biolocomotion at the interface *Annual Review of Fluid Mechanics* (*Annu. Rev. Fluid Mech.*) vol 38 (Annual Reviews) pp 339–69

[37] Anderson D *et al* 2023 Iceberg Project, (https://github.com/danielmanderson/IcebergProject)